



# Modeling the Global Distribution of Solar Wind Parameters on the Source Surface Using Multiple Observations and the Artificial Neural Network Technique

Yi Yang<sup>1,2</sup> · Fang Shen<sup>1,2,3</sup> 

Received: 22 January 2019 / Accepted: 17 July 2019  
© Springer Nature B.V. 2019

**Abstract** The global distribution of magnetic field and other plasma parameters on the source surface, which we set at 2.5 solar radii, is important for coronal and heliospheric modeling. In this article, we introduce a new data-driven self-consistent method to obtain the global distribution of different parameters. The magnetic and polarized brightness ( $pB$ ) observations are used to derive the magnetic field and electron density on the source surface, respectively. Then, an artificial neural network (ANN) machine learning technique is applied to establish an empirical relation among the solar wind velocity, the magnetic field properties, and the electron density. The ANN is trained with global observational data, and is validated to be more reliable than the Wang–Sheeley–Arge (WSA) model for reconstructing the solar wind velocity, especially at high latitudes. The plasma temperature distribution is derived by solving a simplified one-dimensional (1D) magnetohydrodynamic (MHD) equation system on the source surface. Using the method in this study we can obtain the global distribution for all the parameters self-consistently based on magnetic and polarized brightness observations. The modeling results of four Carrington rotations from different solar cycle phases are presented to validate the method.

**Keywords** Source surface · Coronal magnetic field distribution · Coronal polarized brightness distribution · Interplanetary scintillation · Artificial neural network technique

## 1. Introduction

The source surface is an imaginary spherical shell in the corona, where the solar wind velocity and the magnetic field are all assumed to become radial (Altschuler and Newkirk, 1969;

---

✉ F. Shen  
fshen@spaceweather.ac.cn

<sup>1</sup> SIGMA Weather Group, State Key Laboratory of Space Weather, National Space Science Center, Chinese Academy of Sciences, Beijing 100190, China

<sup>2</sup> University of Chinese Academy of Sciences, Beijing 100049, China

<sup>3</sup> HIT Institute of Space Science and Applied Technology, Shenzhen 518055, China

Schatten, Wilcox, and Ness, 1969). The typical height of the source surface is 2.5 solar radii, because this value can best match the magnetic field polarity observed at 1 AU (Hoeksema, Wilcox, and Scherrer, 1983). The solar wind originating in the Sun reaches the Earth a few days later after crossing the source surface. Therefore, the study of the magnetic field and plasma properties on the source surface is significant for the prediction of the characteristics of the space environment near the Earth.

On one hand, the knowledge of the global distribution of the magnetic field and plasma parameters, such as the number density, flow velocity, and plasma temperature on the source surface is important for determining the initial boundary conditions of three-dimensional (3D) magnetohydrodynamic (MHD) models. Many previous studies have shown that more physical and realistic initial boundary conditions could evidently improve the performance of the coronal and heliospheric MHD models (Feng *et al.*, 2010, 2012; Feng, Ma, and Xiang, 2015; Hayashi, 2005; Hayashi *et al.*, 2006; Jackson *et al.*, 2015; Kim *et al.*, 2014; Odstrcil, 2003; Shen *et al.*, 2007, 2018; Wiengarten *et al.*, 2013). On the other hand, the characteristics of the distributions of the parameters on the source surface could be mapped to 1 AU by computational resource-saving methods to give space weather predictions quickly (Riley and Lionello, 2011). Although these methods are much simpler, some of them can have a comparable forecasting performance to the complicated MHD models (Owens *et al.*, 2008; Riley *et al.*, 2006). For example, the Wang–Sheeley–Arge (WSA) model (Wang and Sheeley, 1990; Arge and Pizzo, 2000; Arge *et al.*, 2003), which takes advantage of the negative correlation between the solar wind speed and the expansion factor ( $f_s$ ) of the magnetic field at the source surface can predict the solar wind speed at 1 AU properly. This model has been operational at the Space Weather Prediction Center of the National Oceanic and Atmospheric Administration (SWPC/NOAA). Furthermore, the global structure of ambient solar wind parameters can impact on the modeling and forecasting of more geo-effective transient phenomena, such as coronal mass ejections (CMEs) and shocks (Dryer *et al.*, 2004; Fry *et al.*, 2003; Gopalswamy *et al.*, 2001; Lugaz, Manchester, and Gombosi, 2005; Shen *et al.*, 2013, 2014; Zhao and Dryer, 2014).

Although there are no *in situ* observations near the Sun due to the limitations of space measurements, a lot of research in this topic is still being performed with remote observations and theoretical analyses. The coronal magnetic field is one of the most frequently studied parameters in heliophysics. Many coronal magnetic field models have been developed based on photospheric magnetograms, including potential field models, force-free field models, and coronal MHD models (Linker *et al.*, 1999; Mikic *et al.*, 1999; Riley *et al.*, 2011; Jiang and Feng, 2013). A recent review by Wiegmann, Petrie, and Riley (2017) discussed all of these approaches and pointed out their advantages and disadvantages. The potential field source-surface (PFSS) model is one of the most widely used. It was first developed by Altschuler and Newkirk (1969) and Schatten, Wilcox, and Ness (1969). Then several studies refined the PFSS model. Levine, Schulz, and Frazier (1982) and Schulz, Frazier, and Boucher (1978) studied the effects of a nonspherical source surface. Zhao and Hoeksema (1995) added the effects of current sheets outside the source surface to build the current sheet source-surface (CSSS) model. Arden, Norton, and Sun (2014) and Lee *et al.* (2011) studied the effects of using different source-surface radii. However, the original PFSS model still remains commonly used and its performance is comparable with that of other models (Riley *et al.*, 2006).

The coronal electron density structure is usually deduced from the observation of white-light brightness according to the theory of Thomson scattering. The white-light brightness of the corona could only be measured during total solar eclipses in the past, while now there are regular observations with the help of coronagraphs. A widely used spherically symmetric

inversion method of the coronal electron density was first introduced by Van de Hulst (1950) and was implemented to estimate the density along radial profiles within coronal holes or streamers. Then this method was used to study the two-dimensional (2D) or 3D distribution of the coronal electron density (Quémerais and Lamy, 2002; Wang and Davila, 2014). Frazin and Janzen (2002) developed a solar rotational tomographic approach to obtaining the 3D coronal density. With the high-cadence and multipoint white-light observations provided by recent advanced coronagraphs, some other 3D tomography methods have been developed to reconstruct the coronal density (Kramar *et al.*, 2014; Morgan, 2015; Patoul, Foullon, and Riley, 2015). There are also some studies deriving the coronal density using coronal magnetic field structures (Guhathakurta, Holzer, and Macqueen, 1996; Wang, Young, and Muglach, 2014).

The global structure of the solar wind flow velocity can be obtained from interplanetary scintillation (IPS) observations at the Institute for Space-Earth Environmental Research of Nagoya University. The institute has provided global velocity maps on the source surface for many years by using IPS measurements and tomographic analysis (Kojima *et al.*, 2007; Tokumaru *et al.*, 2010). The IPS measurements have also been used by some solar wind MHD models as boundary conditions (Hayashi *et al.*, 2003; Hayashi, Tokumaru, and Fujiki, 2016; Jackson *et al.*, 2015). However, the ground-based IPS observations are not available for every winter due to thick snowing at the observatories and the data often cannot cover all the points on the source surface (Tokumaru *et al.*, 2017).

The WSA model can give the velocity distribution based on an empirical function, which derives the solar wind speed from both the magnetic field expansion factor ( $f_s$ ) and the minimum angular distance ( $\theta_b$ ) between an open field line footpoint and its nearest coronal hole boundary (Riley, Linker, and Arge, 2015). Since the photospheric magnetic field is regularly measured by many space-based or ground-based instruments, the velocity distribution could always be obtained using the WSA model. However, the empirical function of the WSA model was derived from *in situ* observations only in the ecliptic plane at 1 AU (Arge and Pizzo, 2000). Thus, using the WSA function to deduce the global velocity distribution might have uncertainties, especially at high latitudes.

Most of the previous studies obtain the global structure of different solar wind parameters individually from only one kind of observation. For example, the WSA model determines the solar wind velocity using only magnetic observations. Strachan *et al.* (2012) studied the evolution of plasma parameters on the coronal source surface during solar minimum by analyzing data from the *Solar and Heliospheric Observatory* (SOHO). They produced global maps of outflow velocities and densities on the source surface using the UV and white-light data observed by the *Ultraviolet Coronagraph Spectrometer* (UVCS) and the *Large Angle Spectroscopic Coronagraph* (LASCO), respectively. Nevertheless, a few efforts have been made to construct the global distribution of different parameters self-consistently from multiple observations. The distribution based on multi-observations can be more reliable and can provide more realistic initial boundary condition to 3D MHD solar wind models. Wei *et al.* (2003) conducted a preliminary study to construct the self-consistent distribution of different parameters on the source surface based on the observations of both white-light brightness and the photospheric magnetic field. They studied the global distribution of the coronal mass flux for Carrington rotation (CR) 1742, and then used the result in a 1D MHD model at the source surface to obtain the self-consistent distribution of different solar wind parameters. Shen *et al.* (2010) and Shen, Feng, and Xiang (2012) improved the method of Wei *et al.* (2003) by utilizing  $f_s$  and  $\theta_b$  in the WSA model and then analyzed the basic characteristics of the global distribution for plasma and magnetic field on the source surface during 136 CRs from four different phases of a solar cycle.

In this article, we aim to introduce a new method that using observations of both, photospheric magnetic field and polarized brightness, obtains the self-consistent global distribution of different solar wind parameters, including the magnetic field ( $B$ ), electron density ( $N$ ), flow velocity ( $V$ ), and plasma temperature ( $T$ ) on the source surface. Our new method applies the artificial neural network (ANN) machine learning technique to establish the correlation among the solar wind velocity, the magnetic field properties, and the electron density. The advantage of this correlation is that it is determined from global observations at all latitudes and it involves more properties. After the learning process, we can obtain the global distribution of  $V$  from both magnetic and polarized brightness observations when the IPS observation is unavailable or incomplete. Then, we can deduce the distribution of  $T$  by solving a simplified 1D MHD equation system at the source surface. Therefore, our results for different parameters are self-consistent and all deduced from observational data.

The outline of this article is as follows. In Section 2, we describe the data and methods that we apply for modeling the global distribution of  $B$ ,  $N$ ,  $V$ , and  $T$  using CR 2062 as an example. In Section 3, firstly, we make a detailed analysis of  $V$  during CR 2062, by comparing it with both observations and the WSA model. Then, we show the results of  $B$ ,  $N$ ,  $V$ , and  $T$  for four CRs from different solar cycle phases. In Section 4, we summarize the results and discuss.

## 2. Data and Methods

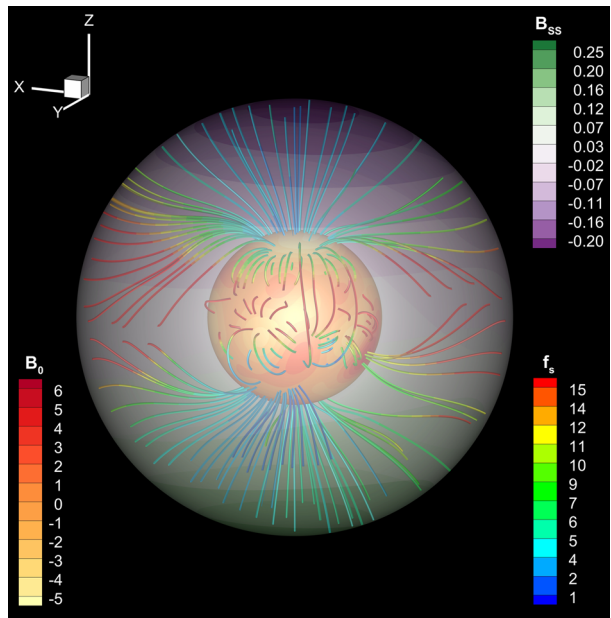
In this section, we introduce the data and methods we apply to obtain the global distributions of the solar wind magnetic field, electron density, flow velocity, and plasma temperature on the source surface. CR 2062 is used in this section as an example.

### 2.1. Magnetic Field

The magnetic field structure is usually the most important property in solar-heliospheric studies since it can control the structure and energy of plasma in the corona and the heliosphere. There are many coronal magnetic field models, as introduced in Section 1. In this article, we choose the commonly used PFSS model, because it requires less computer resources while working as well as more complicated models on reproducing large-scale structures (Riley *et al.*, 2006). The PFSS model has two basic assumptions: i) there is no current in the corona between the solar surface ( $1 R_{\odot}$ ) and an imaginary spherical surface called the source surface ( $R_{ss} = 2.5 R_{\odot}$ ), namely the potential field assumption; ii) the magnetic field becomes purely radial at this source surface, which is considered the “source” of the solar wind outflow. With these assumptions, a photospheric synoptic magnetogram can be used to extrapolate the 3D magnetic field components of the vector  $B(r, \theta, \phi)$  at any point in the region of  $1 R_{\odot} \leq r \leq R_{ss}$ . Tóth, van der Holst, and Huang (2011) presented a detailed explanation of the calculation process.

The time series of full-disk magnetograms can be combined to make a synoptic magnetogram, which gives the global magnetic field at the photosphere. Synoptic maps are provided by many space or ground observatories, such as the Wilcox Solar Observatory (WSO), the *Michelson Doppler Imager* (MDI) instrument on the *Solar and Heliospheric Observatory* (SOHO), the *Helioseismic and Magnetic Imager* on the *Solar Dynamics Observatory* (SDO) and the *Global Oscillation Network Group* (GONG) of the National Solar Observatory (NSO). The quality of the input magnetogram may have influence on the accuracy of the PFSS model (Hayashi, Yang, and Deng, 2016; Liu *et al.*, 2012;

**Figure 1** The 3D magnetic field for CR 2062 deduced from the PFSS model. The magnetic field strength at the photosphere and at the source surface is shown with yellow-to-red and purple-to-green colors, respectively. The rainbow colors used for the magnetic field lines show the magnitude of  $f_s$ , which represents the degree of super-radial expansion.



Riley *et al.*, 2014). According to these studies, we choose the synoptic maps provided by NSO/GONG (<http://gong.nso.edu/>) in this article.

After obtaining the coronal magnetic field strength using the PFSS model, we can derive some other important properties by tracing field lines. The expansion factor ( $f_s$ ) on the source surface can be derived from the function

$$f_s = \left(\frac{B_0}{B_{ss}}\right) \left(\frac{R_\odot}{R_{ss}}\right)^2, \tag{1}$$

where  $B_0$  and  $B_{ss}$  are the magnetic field strengths at the photosphere and at the source surface, respectively. The parameter  $f_s$  measures the rate at which the flux tube expands between the photosphere and the source surface, as compared with a purely radial expansion. Thus, the flux tube expansion is super-radial where the value of  $f_s$  is larger than 1.

Figure 1 presents the 3D magnetic field obtained using the PFSS model for CR 2062. In this figure,  $B_0$  and  $B_{ss}$  are shown with different colors to represent the distribution of the magnetic field strength at the photosphere and at the source surface, respectively. A set of magnetic field lines are also plotted to show the magnetic field structure between the photosphere and the source surface. We can see that most of the open field lines come from the polar regions and most of the closed field lines are located in the low latitude regions. The various colors of the open field lines represent the magnitude of  $f_s$ , which denotes the degree of super-radial expansion. The rainbow colors from blue to red indicate that the  $f_s$  magnitudes vary from small to large. As we can see in Figure 1, the field lines starting from the polar region will remain to be blue if they stay close to the radial direction, while they will gradually turn into red if they bend to the equatorial region.

After tracing magnetic field lines, we can see the regions of open field lines as coronal holes. The property  $\theta_b$  can be obtained by calculating the minimum angular distance between an open field line footpoint and its nearest coronal hole boundary. The  $f_s$  and  $\theta_b$  are both good indicators for the solar wind speed; they have been used in the WSA model for

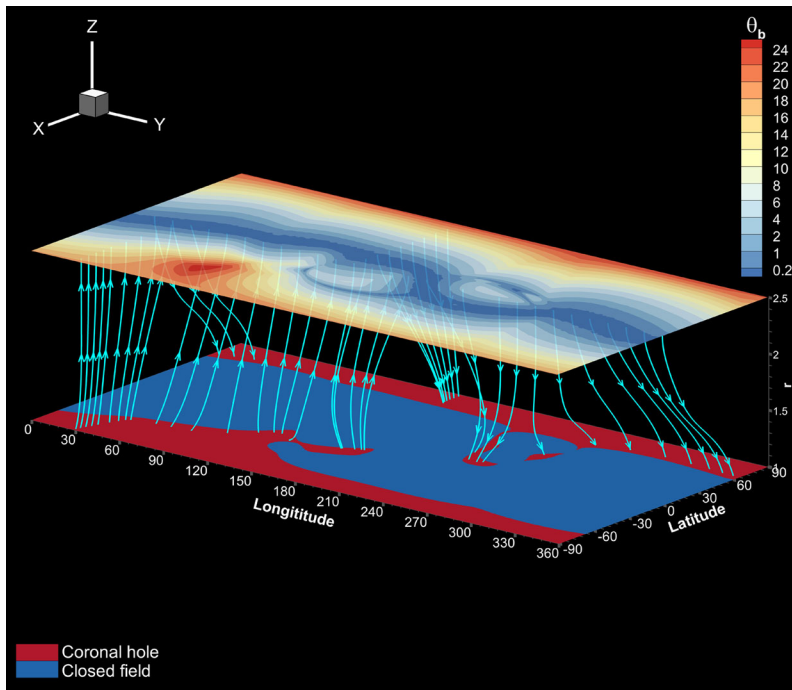


**Figure 2** The distribution of coronal holes on the photosphere and the contour of  $\theta_b$  on the source surface for CR 2062. The magnetic field lines show the connection of the photosphere and the source surface. The arrows indicate the direction of the magnetic field.

years. Riley, Linker, and Arge (2015) made some detailed analyses comparing these two parameters.

In Figure 2, the distribution of coronal holes on the photosphere and the distribution of  $\theta_b$  values on the source surface are presented simultaneously. The coronal hole regions are shown in red color and the closed field in blue. The border between the red and the blue regions indicates the coronal hole boundary. The connection between the photosphere and the source surface can be shown by drawing field lines. We drew some field lines that cross the source surface at the equator and at 30 or 180 degree of Carrington longitude. It is obvious that the smaller  $\theta_b$  value at the source surface connects it with the location closer to the coronal hole boundary at the photosphere, which is reasonable according to the definition of  $\theta_b$ .

We also introduce two other properties, since we will use them in Section 2.3 for determining the solar wind velocity. One is the latitude difference between a point at the source surface and the heliospheric current sheet (HCS). It can be understood as the magnetic latitude, noted as  $L_m$ . The relations of the HCS with the solar wind structure has been studied in several articles (Hoeksema, Wilcox, and Scherrer, 1983; McComas *et al.*, 2006; Newkirk and Fisk, 1985). The other property is the latitude of a footpoint, noted as  $L_0$ . A recent study demonstrated that  $L_0$  can have a relation with the corresponding solar wind velocity (Hofmeister *et al.*, 2018).

Then, we have obtained six magnetic field properties from a PFSS model,  $B_{ss}$ ,  $B_0$ ,  $f_s$ ,  $\theta_b$ ,  $L_m$ , and  $L_0$ . The global distribution maps of these properties on the source surface for CR

2062 are summarized in Figure 3. These properties will be used to determine the solar wind velocity in Section 2.3.

## 2.2. Electron Density

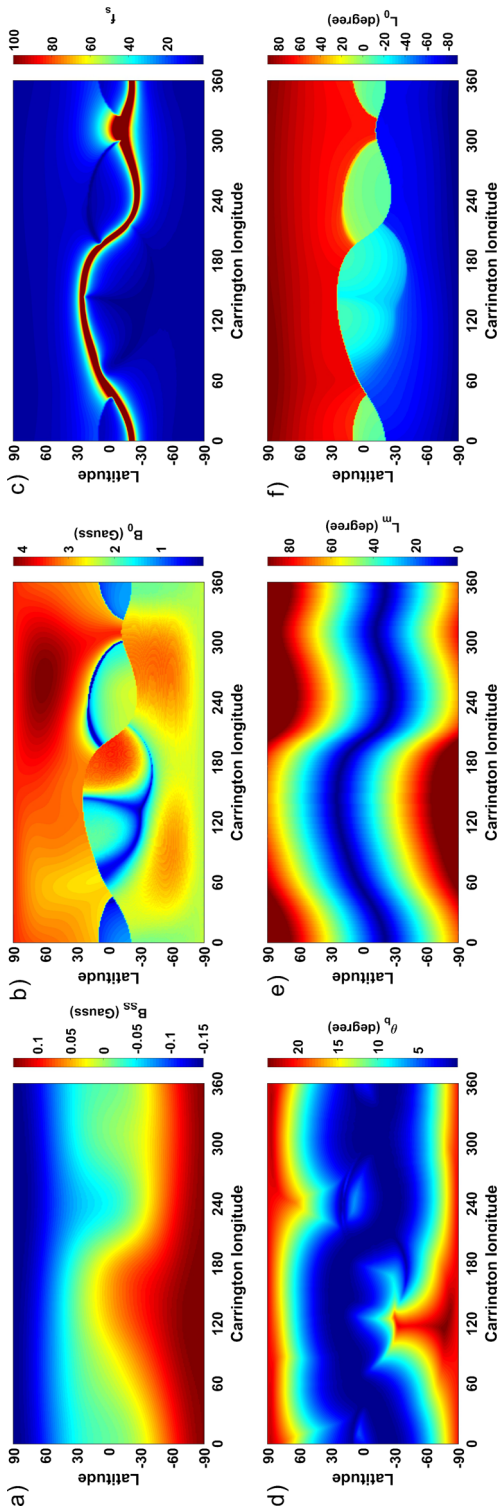
Since the coronal magnetic field is extrapolated from the photospheric observations with some unphysical assumptions, the deduced magnetic field structure in the corona may be not very accurate. The coronal density structure can be regarded as a tracer of the magnetic field morphology, due to the plasma frozen-in effect in the corona (Wiegmann, Petrie, and Riley, 2017). Some studies have shown that the global distribution of the coronal electron density derived from white-light observations can be used to optimize the coronal magnetic field models (Kramar *et al.*, 2014; Jones, Davila, and Uritsky, 2016; Everson and Dikpati, 2017) and provide more reliable initial conditions for solar wind modeling (Patoul, Foullon, and Riley, 2015).

The observed white-light brightness contains three main components, including the instrumental stray light, the K-corona brightness, and the F-corona brightness. The K corona represents the Thomson scattering of photospheric light by free electrons, while the F corona arises from interplanetary dust scattering (Billings, 1966). Thus, the electron density can be deduced from the K-corona brightness. However, it is difficult to separate the K-corona from the F-corona in the total white-light brightness (Hayes, Vourlidas, and Howard, 2001). Since the polarized contribution of the F-corona can be ignored in the low corona (Hayes, Vourlidas, and Howard, 2001; Koutchmy and Lamy, 1985), the inversion of the coronal density is usually based on the  $pB$  observations (Frazin and Janzen, 2002; Quémerais and Lamy, 2002; Van de Hulst, 1950; Wang and Davila, 2014).

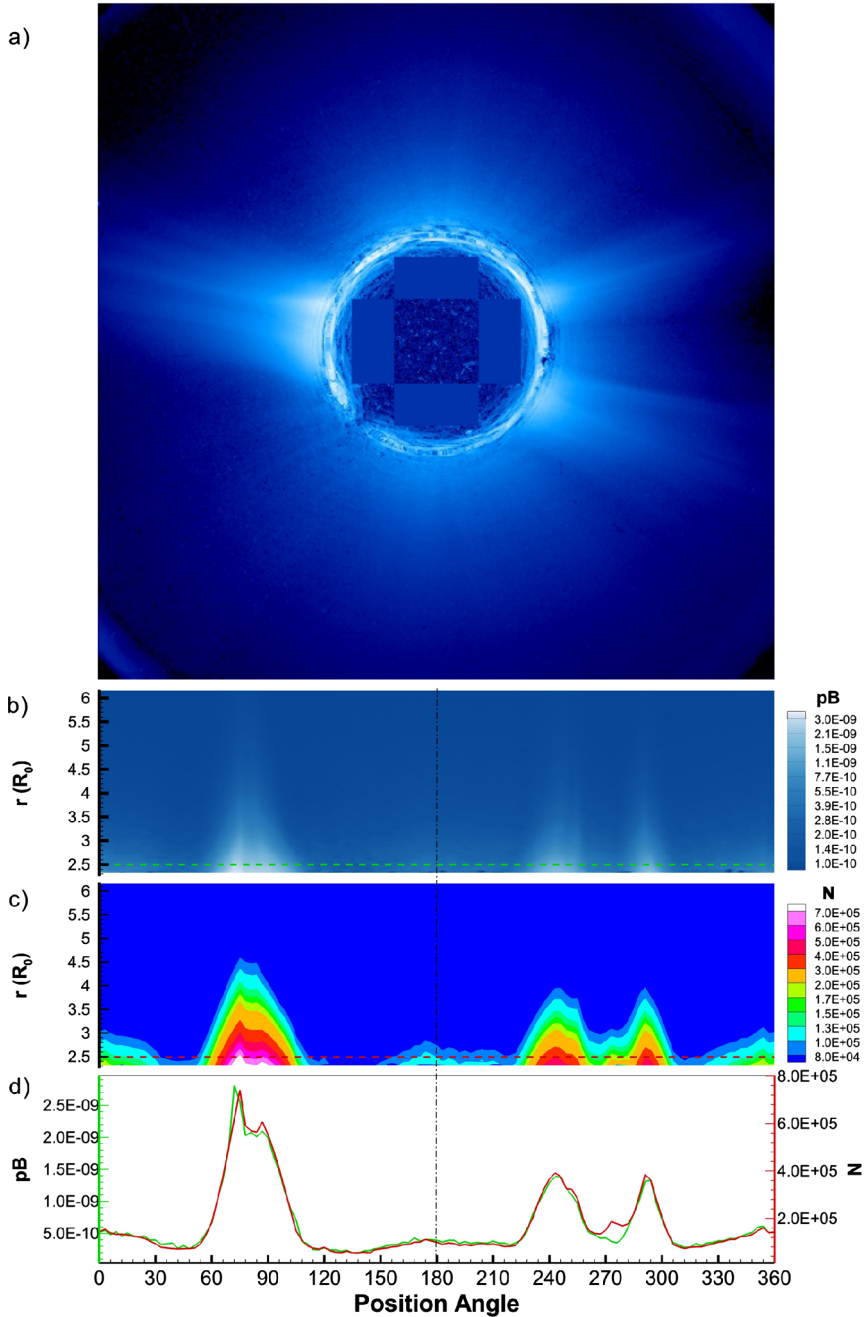
In this article, we apply a commonly used method developed by Van de Hulst (1950) to invert the coronal density from the polarization-brightness observations. This method has been implemented by a set of IDL routines in the Solar SoftWare (SSW, <http://www.lmsal.com/solarsoft/>) library (Freeland and Handy, 1998). The  $pB$  data we use in this study is from the SOHO/LASCO-C2 coronagraph; it can be downloaded from the instrument website (<http://lasco-www.nrl.navy.mil/content/retrieve/polarize/>). The LASCO  $pB$  observations are made regularly once or twice a day. The  $pB$  images of LASCO-C2 has a useful field-of-view (FOV) of about 2.2 to 6.0  $R_{\odot}$  with a resolution of 512 by 512 pixels.

Figure 4a presents the original LASCO-C2  $pB$  image of 21 October 2007 at 21:05 UT, which belongs to CR 2062. We can see the streamers are brighter on the east and west limbs, while the polar regions are much darker. Figure 4b exhibits the values of the same  $pB$  data, but the plot is transformed into polar coordinates, which are more convenient for the inversion process. The horizontal axis is the position angle measured counterclockwise from the north pole and the vertical axis is the radial distance from the solar center. Figure 4c shows the values of the electron density deduced from the  $pB$  data. The comparison of panels b and c indicates a good coincidence in the observed  $pB$  data and the inversed density. We can see that the widths and locations of the streamers are coincident. The profiles of  $pB$  and  $N$  at the source surface are shown simultaneously in Figure 4d. The profiles correspond to the locations indicated by the dashed green and red lines in panels b and c, respectively.

The SSW routines can be used only to calculate the FOV density distribution. To construct the global density distribution on the source surface, we use a time series of the density profiles and obtain a density synoptic map, similar to a magnetic synoptic map. The time series consists of 28 profiles, one for each day of the CR. Each profile records the density variation along the latitude direction. The observation time of these profiles can be converted to Carrington longitudes; then, the profiles are interpolated to all the longitudes



**Figure 3** The global distribution of  $B_{ss}$ ,  $B_0$ ,  $f_s$ ,  $\theta_b$ ,  $L_m$ , and  $L_0$  on the source surface for CR 2062 are shown in **a)**, **b)**, **c)**, **d)**, **e)**, and **f)**, respectively.



**Figure 4** **a)** The original LASCO-C2  $pB$  image of 21 October 2007 at 21:05 UT. **b)** The same  $pB$  data transformed into polar coordinates. The *green dashed line* is the location of the source surface at  $2.5 R_{\odot}$ . **c)** The electron density ( $N$ ) distribution deduced from  $pB$  data in units of  $N$  is  $\text{cm}^{-3}$ . The *red line* is the location of the source surface at  $2.5 R_{\odot}$ . **d)** The profile of the  $pB$  data (*green line*) and derived density (*red line*) at the source surface. The *dash-dotted vertical line* and the *vertical axes* in **b)** to **d)** indicate the boundaries of the east and west limb in **a)**.

**Figure 5** The global distribution of electron density ( $N$ ) on the source surface during CR 2062.

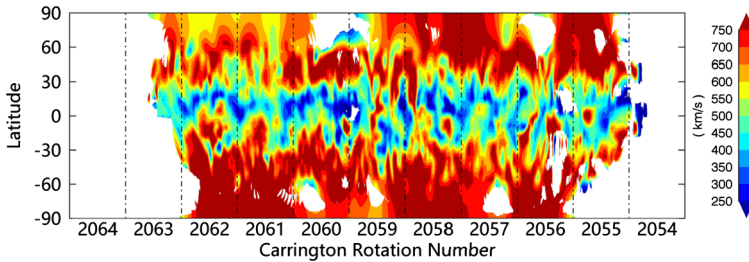
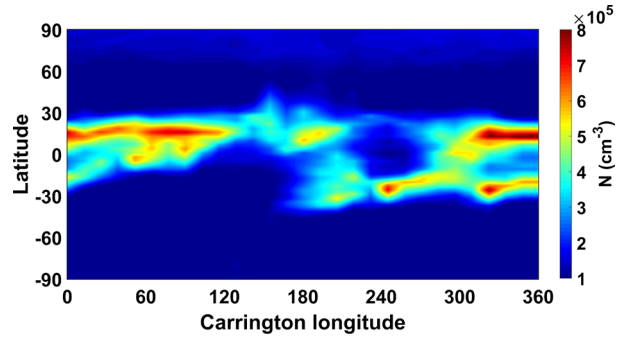


**Figure 6** The IPS observed solar wind velocity distribution on the source surface from CR 2054 to CR 2064 in 2007.

covering from 0 to 360 degree to construct the full synoptic map. Figure 5 shows the global distribution of  $N$  on the source surface we finally obtained for CR2062. The main advantages of this method for obtaining the global density distribution is that it is based on the widely used and validated method of Van de Hulst (1950), the computation is very fast and the uncertainty has been estimated by former studies (Wang and Davila, 2014).

### 2.3. Solar Wind Velocity

The global structure of  $V$  is very important for understanding the solar wind origin and modeling the heliosphere. However, most *in situ* measurements of the solar wind velocity are limited to the ecliptic plane due to the orbits of the spacecraft. *Ulysses* improved our understanding of the 3D structure of  $V$  with *in situ* measurements, but it had stopped working after three pole-to-pole passages. Thus, the information as regards  $V$  at the high latitudes is hard to be obtained directly.

The IPS data of the Nagoya University is one of the few sources providing out-of-ecliptic observations of  $V$ . The data can be downloaded from the official website ([http://stsw1.stelab.nagoya-u.ac.jp/ips\\_data-e.html](http://stsw1.stelab.nagoya-u.ac.jp/ips_data-e.html)). Figure 6 shows the IPS data of the velocity distribution during 2007. The white regions in the plot are due to lack of data. The data missing situation in other years is similar or even worse than in 2007.

The WSA model provides an empirical function between solar wind speed and the two magnetic properties  $f_s$  and  $\theta_b$  (Arge *et al.*, 2003). We can use the WSA function to deduce the global velocity distribution as long as the synoptic magnetograms are available, since the global distribution of  $f_s$  and  $\theta_b$  can be derived from the PFSS model. However, the WSA model can be uncertain for deducing the velocity at high latitudes, as we discussed

in Section 1. Moreover, the WSA function only associates the velocity with photospheric magnetic field data.

Therefore, we aim to use the available IPS observations to establish an empirical relation among the velocity, magnetic field properties, and the electron density. In this way, we can always obtain the velocity using magnetograms and  $pB$  data and we can probably have more reliable results at the out-of-ecliptic latitudes.

Tokumaru *et al.* (2017) studied the linear relation between the coronal hole area and  $V$  using IPS data. They also derived a linear relation between the expansion factor and  $V$ . It should be noted that the expansion factor in their study is given for each coronal hole, while the  $f_s$  in this work is calculated for each field line following the WSA model. Wintoft and Lundstedt (1997, 1999) used the artificial neural network (ANN) technique to predict the daily-averaged solar wind velocity at 1 AU. In this study, we use the ANN machine learning method as in our previous work (Yang *et al.*, 2018) to obtain the global distribution of  $V$  on the source surface. In this article, we only briefly describe the application of this method.

The architecture of our ANN in this study is a three-layer feedforward network. The calculation of our ANN can be expressed as follows:

$$y = g \left( b_0 + \sum_{j=1}^n v_j f_j \left( b_j + \sum_{i=1}^m w_{ji} x_i \right) \right), \tag{2}$$

where  $x_i$  are the input parameters,  $w_{ji}$ ,  $v_j$ ,  $b_j$ , and  $b_0$  are the weights and biases to be learned,  $f_j$  and  $g$  are activation functions between the ANN layers,  $y$  is the output target,  $g$  is a linear function, and  $f_j$  is a bipolar sigmoid nonlinear activation function defined by

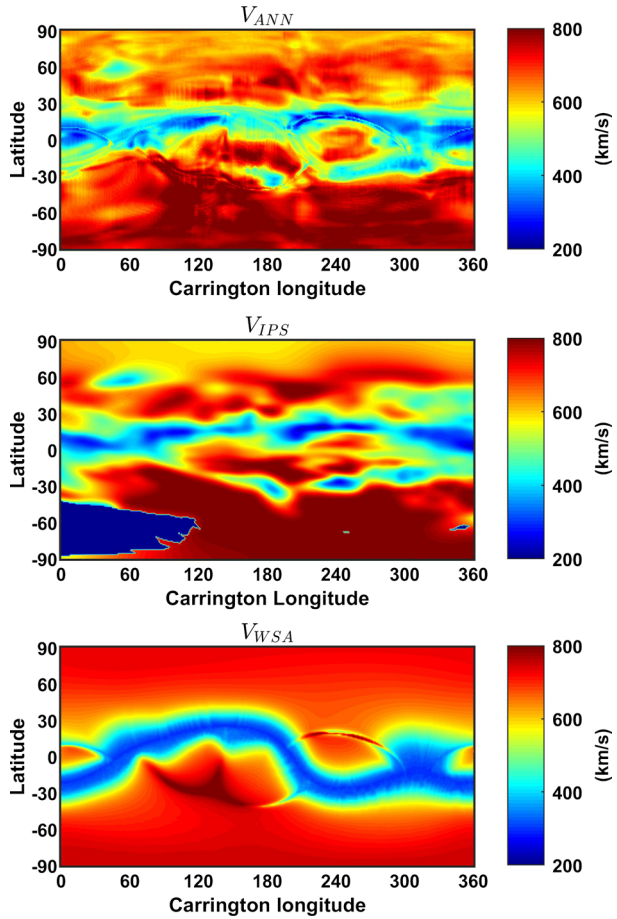
$$f(x) = \frac{2}{1 + e^{-2x}} - 1. \tag{3}$$

In order to establish the new relation for  $V$ , we use the IPS velocity data as the output target  $y$ , the magnetic properties ( $B_{ss}$ ,  $B_0$ ,  $f_s$ ,  $\theta_b$ ,  $L_m$ , and  $L_0$ ) obtained in Section 2.1, and the density  $N$  obtained in 2.2 as the input parameters  $x_i$ . Then we can obtain the optimized weights and biases after a machine learning process. Finally, we apply the ANN model to calculate  $V$  on the source surface.

Since the global structure of  $V$  varies with the solar cycle, we train the ANN to obtain a specific relation for each of the four solar phases. The descending phase is trained using the data from CR 2057 to CR 2062 during 2007. The minimum phase is trained using the data from CR 2070 to CR 2072 and CR 2083 to CR 2084 from 2008 to 2009. The ascending phase is trained using the data of CR 2111, CR 2112 and CR 2115 during 2011. The maximum phase is trained using the data from CR 2138 to CR 2139 and CR 2151 to CR 2152 from 2013 to 2014. These periods are selected for training because the IPS data have a better spatial coverage for all latitudes. The regions missing IPS data are excluded in the training process.

The top panel of Figure 7 exhibits the global distribution of  $V$  during CR 2062 obtained from our ANN model. The  $V$  distributions from IPS observation and the WSA model are also shown in Figure 7 as a preliminary validation of our result. In the following, we note the  $V$  obtained using IPS data as  $V_{IPS}$ , the  $V$  modeled by our ANN as  $V_{ANN}$ , and the  $V$  modeled by the WSA model as  $V_{WSA}$ , respectively. Firstly, we can see that the large-scale variations in the three panels agree with each other qualitatively. Both  $V_{ANN}$  and  $V_{WSA}$  have higher values at the polar regions and lower values near the equator, which agrees with the IPS observations. We note that the deep blue color at the lower-left corner in the middle

**Figure 7** The solar wind velocity distribution on the source surface for CR 2062 obtained from our ANN model (top), the IPS observation (middle) and the WSA model (bottom).



panel is due to the lack of IPS data. The  $V_{ANN}$  in the top panel is properly modeled in the region with no IPS observation, which demonstrates the generalization of the ANN model. This also implies that the ANN method can be used to fill the missing IPS data. Secondly, it seems that  $V_{ANN}$  has more details than  $V_{WSA}$ . In Section 3.1, we will make some further analyses of these results. It should be noted that the  $V_{WSA}$  in this study is calculated using the following function:

$$V_{WSA} = V_s + \frac{V_f}{(1 + f_s)^{a_1}} \left[ 1 - 0.8 \exp\left(-\left(\frac{\theta_b}{a_2}\right)^{a_3}\right) \right]^{a_4}, \tag{4}$$

where  $V_s = 250 \text{ km s}^{-1}$ ,  $V_f = 675 \text{ km s}^{-1}$ ,  $a_1 = 2/9$ ,  $a_2 = 2$ ,  $a_3 = 1$ ,  $a_4 = 1$ . These values are determined in accordance with GONG data used in this article, while different values may be used by other studies (MacNeice, 2009; Riley, Linker, and Arge, 2015).

### 2.4. Plasma Temperature

The temperature is also one of the important plasma parameters that are necessary for providing initial boundary conditions for coronal and heliospheric modeling. The 3D MHD

models often use a uniform or initial boundary condition for  $T$ . However, a more reliable  $T$  with observational constraints could improve the modeling results (Hayashi *et al.*, 2006).

In this article, we derive the global distribution of  $T$  by solving a self-consistent MHD system on the source surface. The ideal MHD equations can be simplified to 1D at the source surface as follows:

$$V \frac{\partial N}{\partial r} + N \frac{\partial V}{\partial r} + \frac{2NV}{r} = 0, \tag{5}$$

$$NV \frac{\partial V}{\partial r} + \frac{\partial p}{\partial r} + Ng = 0, \tag{6}$$

$$N \frac{\partial p}{\partial r} - \gamma p \frac{\partial N}{\partial r} = 0, \tag{7}$$

$$r \frac{\partial B}{\partial r} + 2B = 0, \tag{8}$$

$$p = 2NR'T, \tag{9}$$

$$\frac{\partial p}{\partial r} = 2R'T \frac{\partial N}{\partial r} + 2R'N \frac{\partial T}{\partial r}, \tag{10}$$

$$\beta(B) = 8\pi p/B^2. \tag{11}$$

In this set of equations,  $r$  is the solar radius,  $p$  is the pressure,  $g$  is the gravitational constant,  $\gamma$  is the polytropic index, and  $\beta$  is the plasma beta. The previous equations are the same used by Shen *et al.* (2010) and Shen, Feng, and Xiang (2012). The only difference is that we do not need the extra statistical mass flux to close the equations. Equations 5 to 10 are well-known, while Equation 11 corresponds to plasma  $\beta$ . Therefore, we have seven equations, and 10 variables including  $B$ ,  $N$ ,  $V$ ,  $T$ ,  $p$ ,  $\frac{\partial B}{\partial r}$ ,  $\frac{\partial N}{\partial r}$ ,  $\frac{\partial V}{\partial r}$ ,  $\frac{\partial T}{\partial r}$ , and  $\frac{\partial p}{\partial r}$ . We have obtained three of the variables namely  $B$ ,  $N$ , and  $V$  in Sections 2.1, 2.2, and 2.3, respectively. Thus, we can substitute them in the seven equations above to solve out the seven unknown variables including  $T$ . The gradients can further be used to construct the initial values along the radial direction. The value of plasma beta is empirically determined as:

$$\beta = \begin{cases} \beta_c & \text{(other region)} \\ \frac{C}{B^2} & \text{(current sheet region)}, \end{cases} \tag{12}$$

where  $\beta_c$  and  $C$  are constants. For CR 2062, we used  $\beta_c = 2$  and  $C = 0.01 \text{ G}^2$ , which are reasonable according to the study of Gary (2001). We note the current sheet region as the region where  $B$  is less than 0.05 G. Figure 8 presents the modeling result for  $T$  on the source surface for CR 2062. This figure illustrates that the  $T$  distribution is coupled with the observational information from both  $B$  and  $N$ .

### 3. Results

In this section, we present some results obtained with the method introduced in Section 2. Firstly, we analyze the distribution of  $V$  for CR 2062 particularly in Section 3.1 by comparing it with both the IPS observations and the WSA model. Then, we present the modeling results of  $B$ ,  $N$ ,  $V$ , and  $T$  for four CRs from different solar cycle phases in Section 3.2.

**Figure 8** The modeling result of the plasma temperature distribution on the source surface for CR 2062.

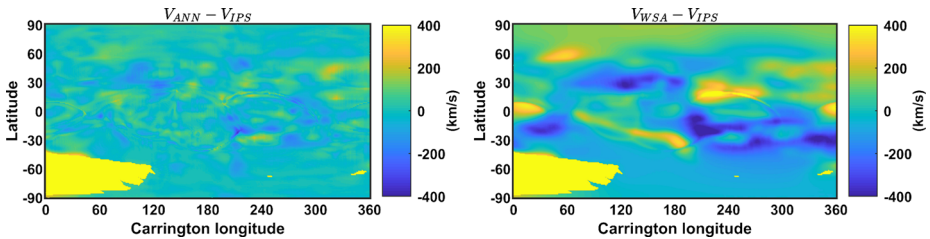
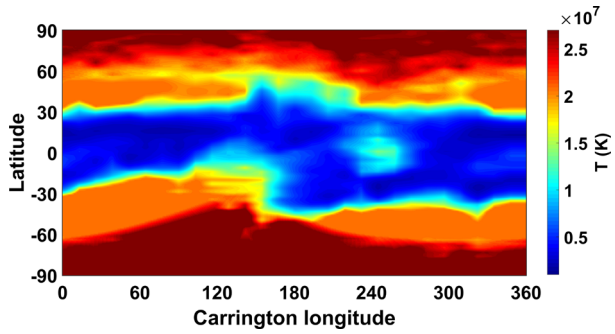


**Figure 9** Plots of the difference between  $V_{ANN}$  and  $V_{IPS}$  (left panel) and the difference between  $V_{WSA}$  and  $V_{IPS}$  (right panel). Both plots are the results for CR 2062.

### 3.1. Analyses of $V$ Obtained from the ANN Model for CR 2062

We have already obtained the global distribution of  $V$  for CR 2062 in Section 2.3, in this section we make some further analyses of the result. In order to examine if our ANN model had rebuilt the global structure of  $V$  properly, we calculate the difference between the modeled value  $V_{ANN}$  and the observed value  $V_{IPS}$  for every grid point (181 by 361 points in this study) on the source surface as shown in the left panel of Figure 9. The difference between  $V_{WSA}$  and  $V_{IPS}$  is presented simultaneously in the right panel of Figure 9 for comparison. In this figure, the yellow color represents the positive difference, while the blue color represents the negative difference. A darker color means a bigger difference value, so it is obvious where the results are worse or better. The darkest yellow regions with difference values of more than 400 (mostly located latitudes  $-30$  to  $-90$ , longitudes  $0$  to  $120$  degree) in both panels are due to missing IPS data. The  $V_{IPS}$  at these missing data points is set to zero, but the  $V_{ANN}$  and  $V_{WSA}$  at these points are filled by the model, so the difference values of  $(V_{ANN}-V_{IPS})$  and  $(V_{WSA}-V_{IPS})$  are all very large. In the left panel of Figure 9, there is no very dark colors at all latitudes, which means a good reconstruction of the global distribution by the ANN model. From the right panel of Figure 9, it can be seen that the WSA model generally overestimated the velocity in the northern polar regions and underestimated the velocity in the southern polar regions. Moreover, there are some large difference values represented in dark yellow and dark blue at the middle and low latitudes ( $0$  to  $\pm 60$  degree) in the right panel, meaning that these regions are not well reconstructed by the WSA model. On the contrary, the difference values for the ANN model are distributed more uniformly and limited to relatively small values.

Figure 10 plots histograms for the difference values excluding the missing data points in Figure 9. This figure shows the difference values quantitatively. The left panel shows that the errors between  $V_{ANN}$  and  $V_{IPS}$  are almost all distributed in the range of  $\pm 200 \text{ km s}^{-1}$  and that

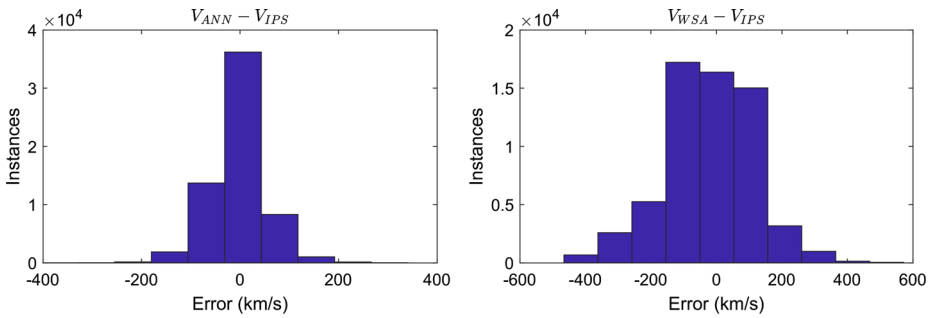


**Figure 10** Histograms of the difference values between  $V_{ANN}$  and  $V_{IPS}$  (left panel) and between  $V_{WSA}$  and  $V_{IPS}$  (right panel). Both panels are the results for CR 2062.

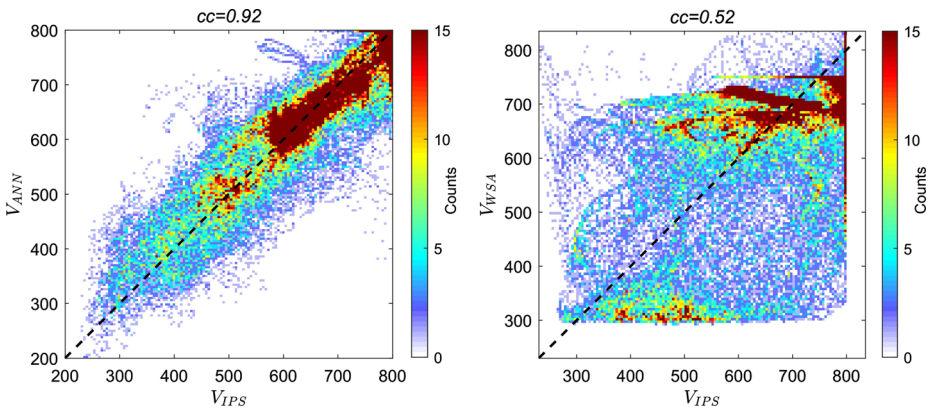


**Figure 11** The left panel is the scatter density plot to compare  $V_{ANN}$  with  $V_{IPS}$ , while the right panel is the scatter density plot to compare  $V_{WSA}$  with  $V_{IPS}$ . The correlation coefficient ( $cc$ ) values are also shown at the top of both panels. Both panels are results for CR 2062.

more than 35,000 points of the total 61,492 points have an error less than  $\pm 50 \text{ km s}^{-1}$ . While in the right panel, the errors between  $V_{WSA}$  and  $V_{IPS}$  are also mostly distributed between  $\pm 200 \text{ km s}^{-1}$ , there are few large errors between  $\pm 200$  and  $\pm 400 \text{ km s}^{-1}$ . This is coincident with Figure 9, because both models give the large-scale structure properly, but the ANN model is more accurate in some regions.

The linear correlation analyses for our ANN model and the WSA model are shown in Figure 11. The black dashed lines in both panels of Figure 11 present the correlation coefficients ( $cc$ ) between the modeled and the observed values equal to 1. The scatter density in the left panel illustrates the correlation between  $V_{ANN}$  and  $V_{IPS}$  and the scatter density in the right panel presents the correlation between  $V_{WSA}$  and  $V_{IPS}$ . The dots of our ANN model are very close to the black dashed line, while the dots of the WSA model are closer to a bimodal structure with two concentrated values at about  $700 \text{ km s}^{-1}$  and  $300 \text{ km s}^{-1}$ . The calculated  $cc$  between  $V_{ANN}$  and  $V_{IPS}$  is 0.92, while the  $cc$  between  $V_{WSA}$  and  $V_{IPS}$  is 0.52, as shown on top of the panels in Figure 11. The  $cc$  value of the WSA model is reasonable according to previous studies (Owens *et al.*, 2008, 2013; Bussy-Virat and Ridley, 2014; Reiss *et al.*, 2016). It should be noted that the IPS velocity might have some uncertainties and can be biased from the real values sometimes. Firstly, the original IPS observations con-

tain the integral effect along line-of-sight, thus the velocity is derived through a tomographic procedure which will bring in some uncertainties. Secondly, the  $V_{\text{IPS}}$  data on the source surface are calculated kinematically without considering the stream-stream interaction and the acceleration process. These uncertainties might be responsible for the relatively lower but still good  $cc$  between  $V_{\text{WSA}}$  and  $V_{\text{IPS}}$ .

With the analyses done, we conclude that our ANN model reconstructed the global distribution of  $V$  quite accurately for CR 2062. Comparisons with the WSA model demonstrated that the global distribution of  $V$  from our ANN model is more reliable.

### 3.2. The Global Distribution of $B$ , $N$ , $V$ , and $T$ for Four CRs from Different Solar Cycle Phases

The global structure of the solar wind parameters varies largely with the solar activity cycle. Thus, it is necessary to test if our model can work for different phases during a solar cycle. We modeled the global distribution of  $B$ ,  $N$ ,  $V$ , and  $T$  for four example CRs from different phases of the solar cycle, namely CR 2062 from the descending phase, CR 2075 from solar minimum, CR 2111 from the ascending phase, and CR 2152 from solar maximum. The modeling results are shown together in Figure 12.

Firstly, we look at the different parameters for every CR by looking at the columns. It is clear that the global distribution of  $V$  and  $T$  deduced by our method is highly coupled with the observationally determined  $B$  and  $N$  for each CR. The magnetic field is the main controller of the large-scale structure. Although the results of  $B$  and  $N$  are derived from different observations, they coincide nicely in the large scale. The highest density and lowest velocity regions are consistent with the current sheet regions. The derived  $V$  and  $T$  are also coincident with each other, as we can see the higher  $V$  generally corresponds to the higher  $T$ .

Secondly, we can look at each parameter for different CRs, looking at the rows. In this way, we can find how the global structure of each parameter changes with the solar cycle. It is obvious that the structures for all the parameters are simpler in the descending and minimum phases, as shown in the first and second columns. The distributions become much more complicated in the ascending and maximum phases. As a typical coronal magnetic field structure, the current sheet becomes wavier during more active solar phases. The classical bimodal structure of  $V$  can be found for CR 2062 and CR 2075, showing higher values at polar regions and lower values near the equator. On the contrary, the structures of  $V$  during CR 2111 and CR 2152 are very complicated with no symmetrical distribution. We can also see that the values of  $V$  and  $T$  during solar maximum are generally lower than the ones during solar minimum. This is coincident with *in situ* observations of *Ulysses* and can be explained by the presence of smaller coronal holes during solar maximum. Thus, our modeling results for the four example CRs agree with the general characteristics of the different solar cycle phases.

To validate further our modeling results, the distributions on the source surface are mapped to 1 AU to be compared with *in situ* observations. The mapping process is based on the simple assumption that the solar wind would remain having a constant speed along the radial direction. Figure 13 exhibits the comparison between our modeling results and the *in situ* observations near Earth. The near-Earth solar wind data is downloaded from the OMNI web interface (<http://omniweb.gsfc.nasa.gov>). The four rows from the top to the bottom, respectively, show the results for the interplanetary magnetic field (IMF) polarity,  $N$ ,  $V$ , and  $T$ . In this article, a positive IMF polarity indicates that the IMF is directed from the Sun to the Earth. The IMF polarities are generally well predicted for all four CRs, which

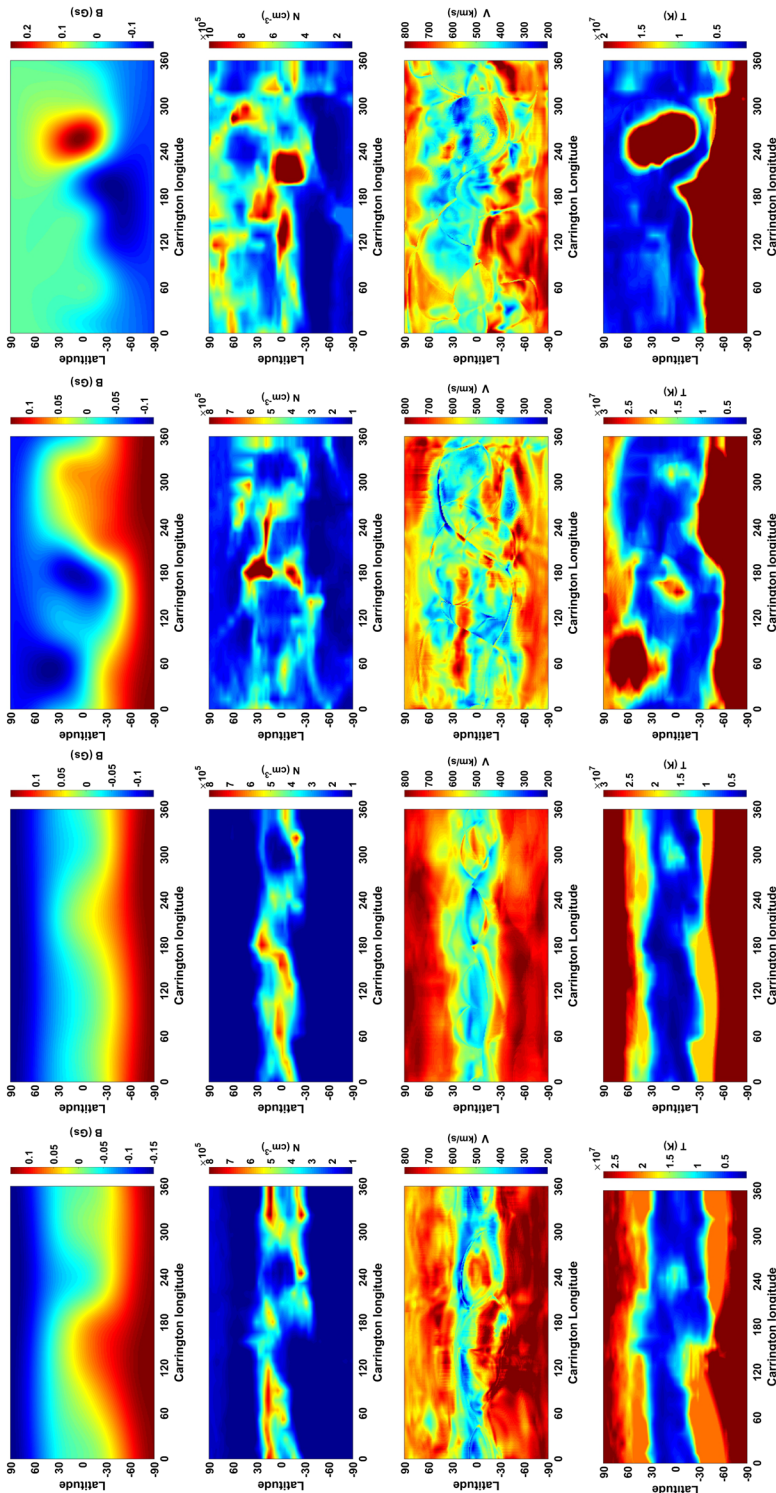


**Figure 12** The global distribution of  $B$  (top row),  $N$  (second row),  $V$  (third row), and  $T$  (bottom row) on the source surface for CR 2062 (first column), CR 2075 (second column), CR 2111 (third column), and CR 2152 (fourth column), respectively.

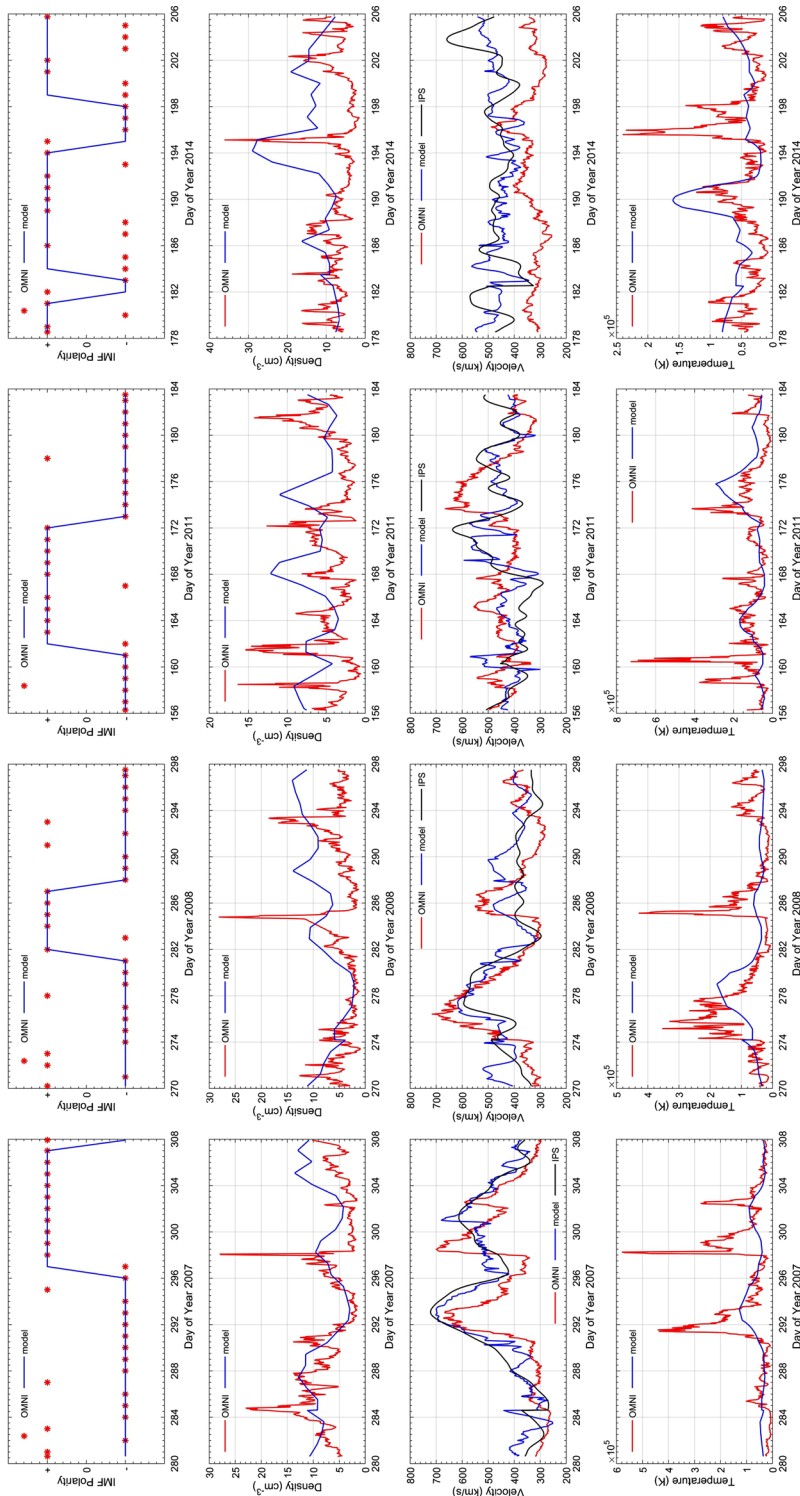


**Figure 13** The comparison between our modeling results and the OMNI data near the Earth for the IMF polarity (*top row*), *N* (*second row*), *V* (*third row*), and *T* (*bottom row*) during CR 2062 (*first column*), CR 2075 (*second column*), CR 2111 (*third column*), and CR 2152 (*fourth column*), respectively.

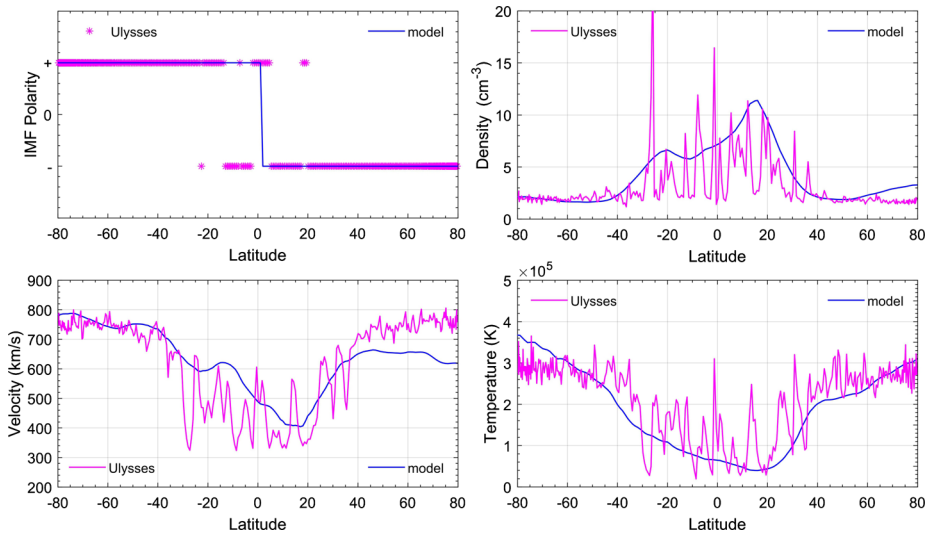


**Figure 14** The comparison between our modeling results for CR 2062 and the *Ulysses* third-orbit data for the IMF polarity,  $N$ ,  $V$ , and  $T$ , respectively.

means that the large-scale structures are modeled correctly. The result for CR 2152 is the worst, which might be because the PFSS model is not suitable for some periods during solar maximum. The velocity results from our model are compared with the OMNI and IPS data simultaneously in the third row of Figure 13. The OMNI and IPS observations are relatively coincident, but they have some discrepancies for small structures and absolute values. Our modeled  $V$  values agree well with the OMNI data during CR 2062 and CR2075, when the IPS data is very close to the OMNI data. The modeled  $V$  values during CR 2111 and CR 2152 are coincident with the IPS data better than with the OMNI data. These results are reasonable, since our model is trained using the IPS observations. The modeling results of  $N$  and  $T$  agree well with the OMNI data on the large scale during all the examined CRs. Most observed peaks of  $N$  and  $T$  are captured by our model, although the specific values may have some difference. Running an MHD model, instead of the simple mapping process, may further improve the prediction of the parameters near the Earth, because dynamic processes such as the interaction between fast and slow streams are ignored with the simple mapping.

The comparison with the near-Earth observations can only validate the modeling results near the ecliptic plane, thus we also compare the results with the *Ulysses* observation to examine our model performance at high latitudes. The third orbit of *Ulysses* spacecraft completed a rapid pole-to-pole (about  $-80$  to  $80$  degree) passage in 2007, so the observed data can be used to verify our modeling results for CR 2062. Both the modeled source surface distributions and *Ulysses* data are mapped to 1 AU for comparison. Figure 14 presents the comparison between the CR averaged modeling results for CR 2062 and the *Ulysses* data for the IMF polarity,  $N$ ,  $V$ , and  $T$ , respectively. It can be seen that all the modeled parameters agree with the *Ulysses* observations on the large scale. The modeled results are much smoother than *Ulysses* data, since *Ulysses* data actually contain the variations during many CRs. The modeled and observed IMF polarities are coincident at most latitudes and both show that the inversion of the polarity happens near the equator. The modeled results show higher values of  $N$  at lower latitudes and higher values of  $V$  and  $T$  at higher latitudes, which are also in good agreement with the observations. Both our results and *Ulysses* data show

high density above  $5 \text{ cm}^{-3}$  distributed within  $\pm 20$  degree, velocity larger than  $600 \text{ km s}^{-1}$ , and temperature larger than  $2 \times 10^5 \text{ K}$  distributed above  $\pm 40$  degrees. The comparisons with both the OMNI and *Ulysses* data demonstrate that our model could give the global distribution of different solar wind parameters on the source surface properly.

## 4. Conclusions

In this article, we present a new method to construct the global distribution of  $B$ ,  $N$ ,  $V$ , and  $T$  on the source surface. The distribution of  $B$  is extrapolated from photospheric magnetogram observations using the PFSS model. The distribution of  $N$  is deduced from  $pB$  observations. The distribution of  $V$  is obtained with an ANN model, which establishes the relation among  $V$ , the magnetic field properties, and  $N$ . The ANN is trained using global observations, so it is suitable at all latitudes. After the training process,  $V$  can be deduced based on magnetograms and  $pB$  observations. Finally,  $T$  is derived self-consistently by solving a 1D MHD system on the source surface. In this way,  $T$  is also deduced from magnetograms and  $pB$  observations. Therefore, our method can use the magnetograms and  $pB$  observations to construct the self-consistent global distribution of  $B$ ,  $N$ ,  $V$ , and  $T$ .

The global distribution of  $V$  obtained by our ANN model for CR 2062 is analyzed particularly to show the model performance. The modeled global distribution of  $V$  agrees well with the IPS observations according to the point-by-point difference analysis. Although the ANN architecture we used in this article is relatively simple, the  $cc$  for our modeled and the observed  $V$  is as high as 0.92, which means the ANN can reproduce most of the observed variability. The comparison with the WSA model shows the ability of our ANN model to give a more reliable distribution at all latitudes. The physical mechanism of solar wind acceleration and interaction in the corona is very complicated and has not been fully understood, so the WSA function which relies on only two coronal hole related characteristics,  $f_x$  and  $\theta_b$ , is definitely not enough to model out all the details for the global variation of  $V$ . The ANN technique is a predominant tool for modeling nonlinear complex systems, such as the solar-terrestrial environment. The ANN with a nonlinear active function in the hidden layer can simulate any nonlinear process with suitable input characteristics and proper artificial neurons. The better reconstruction of  $V$  demonstrates that our ANN has reflected the physical process of the solar corona more realistically than the WSA model by involving more theoretical and observational parameters, including  $B_{ss}$ ,  $B_0$ ,  $L_m$ ,  $L_0$ , and  $N_{ss}$ . However, the physical process is still not clear, as it is implicit in the weights and biases of the ANN. Further study is needed for understanding how each parameter we use affects the distribution of  $V$ . In addition, the ANN machine learning technique could train a better model with more sample data. Thus, the performance of the ANN in this article may be improved with more observational data collected in the future.

The modeling results of  $B$ ,  $N$ ,  $V$ , and  $T$  for four CRs from different solar cycle phases are reasonable. The modeled global distributions of different parameters are associated with observations, are self-consistent and solar cycle dependent. The rough comparison of the modeling results with both the near-Earth and *Ulysses* data further validate the performance of our model during the different solar cycle phases. In a future work, we plan to use the global distribution of magnetic field and plasma parameters obtained by this observation-based self-consistent method as a more realistic boundary condition for 3D MHD solar wind modeling.

**Acknowledgements** The data for this work are available at the official websites of NSO/GONG, SOHO/LASCO, and IPS group at Nagoya University. We acknowledge the use of them. The Global Oscillation Network Group (GONG) magnetograms are downloaded from the website of the National Solar Observatory (NSO, <http://gong.nso.edu/>). SOHO is a joint mission of international cooperation between ESA and NASA. The SOHO/LASCO data used here are produced by a consortium of the Naval Research Laboratory (USA), Max-Planck-Institut fuer Astronomie (Germany), Laboratoire d'Astronomie (France), and the University of Birmingham (UK). The polarized brightness ( $pB$ ) data can be downloaded from the LASCO instrument website at NRL (<http://lasco-www.nrl.navy.mil/content/retrieve/polarize/>). The IPS data is provided by the solar wind group at the Institute for Space-Earth Environmental Research (ISEE), Nagoya University, and can be downloaded from the official website ([http://stsw1.stelab.nagoya-u.ac.jp/ips\\_data-e.html](http://stsw1.stelab.nagoya-u.ac.jp/ips_data-e.html)). We acknowledge the use of the OMNIWeb service provided by the NASA/GSFC Space Physics Data Facility. The *Ulysses* and near-Earth *in situ* data in this work are both obtained from the web interface at <http://omniweb.gsfc.nasa.gov>. This work is jointly supported by grants from the National Natural Science Foundation of China (41774184, 41474152, 41731067, and 41531073) and the Specialized Research Fund for State Key Laboratories. FS is also supported by the National Program for Support of Top-notch Young Professionals. The calculations were performed on TianHe-1 (A) at the National Supercomputer Center in Tianjin, China. We thank the editor and the anonymous reviewer for the suggestions that greatly improved this article.

**Disclosure of Potential Conflicts of Interest** The authors declare that they have no conflicts of interest.

**Publisher's Note** Springer Nature remains neutral with regard to jurisdictional claims in published maps and institutional affiliations.

## References

- Altschuler, M.D., Newkirk, G.: 1969, *Solar Phys.* **9**, 131. DOI.
- Arden, W.M., Norton, A.A., Sun, X.: 2014, *J. Geophys. Res. Space Phys.* **119**, 1476. DOI.
- Arge, C.N., Pizzo, V.J.: 2000, *J. Geophys. Res. Space Phys.* **105**, 10465. DOI.
- Arge, C.N., Odstrcil, D., Pizzo, V.J., Mayer, L.R.: 2003, *AIP Conf. Proc.* **679**, 190. DOI.
- Billings, D.E.: 1966, *A Guide to the Solar Corona*, Academic Press, New York.
- Bussy-Virat, C.D., Ridley, A.J.: 2014, *Space Weather* **12**, 337. DOI.
- Dryer, M., Smith, Z., Fry, C., Sun, W., Deehr, C., Akasofu, S.I.: 2004, *Space Weather* **2**, S09001. DOI.
- Everson, R.W., Dikpati, M.: 2017, *Astrophys. J.* **850**, 152. DOI.
- Feng, X., Ma, X., Xiang, C.: 2015, *J. Geophys. Res. Space Phys.* **120**, 10. DOI.
- Feng, X., Yang, L., Xiang, C., Wu, S.T., Zhou, Y., Zhong, D.: 2010, *Astrophys. J.* **723**, 300. DOI.
- Feng, X., Jiang, C., Xiang, C., Zhao, X., Wu, S.T.: 2012, *Astrophys. J.* **758**, 62. DOI.
- Frazin, R.A., Janzen, P.: 2002, *Astrophys. J.* **570**, 408. DOI.
- Freeland, S.L., Handy, B.: 1998, *Solar Phys.* **182**, 497. DOI.
- Fry, C., Dryer, M., Smith, Z., Sun, W., Deehr, C., Akasofu, S.I.: 2003, *J. Geophys. Res. Space Phys.* **108**, 1070. DOI.
- Gary, G.A.: 2001, *Solar Phys.* **203**, 71. DOI.
- Gopalswamy, N., Lara, A., Yashiro, S., Kaiser, M.L., Howard, R.A.: 2001, *J. Geophys. Res. Space Phys.* **106**, 29207. DOI.
- Guhathakurta, M., Holzer, T.E., Macqueen, R.M.: 1996, *Astrophys. J.* **458**, 817. DOI.
- Hayashi, K.: 2005, *Astrophys. J. Suppl.*, **161**, 480. DOI.
- Hayashi, K., Tokumaru, M., Fujiki, K.: 2016, *J. Geophys. Res. Space Phys.* **121**, 7367. DOI.
- Hayashi, K., Yang, S., Deng, Y.: 2016, *J. Geophys. Res. Space Phys.* **121**, 1046. DOI.
- Hayashi, K., Benevolenskaya, E., Hoeksema, T., Liu, Y., Zhao, X.P.: 2006, *Astrophys. J. Lett.* **636**, L165. DOI.
- Hayashi, K., Kojima, M., Tokumaru, M., Fujiki, K.I.: 2003, *J. Geophys. Res. Space Phys.* **108**, 1102. DOI.
- Hayes, A.P., Vourlidas, A., Howard, R.A.: 2001, *Astrophys. J.* **548**, 1081. DOI.
- Hoeksema, J.T., Wilcox, J.M., Scherrer, P.H.: 1983, *J. Geophys. Res. Space Phys.* **88**, 9910. DOI.
- Hofmeister, S.J., Veronig, A., Temmer, M., Vennerstrom, S., Heber, B., Vrsnak, B.: 2018, *J. Geophys. Res. Space Phys.* **123**, 1738. DOI.
- Jackson, B.V., Odstrcil, D., Yu, H.S., Hick, P.P., Buffington, A., Mejia-Ambriz, J.C., Kim, J., Hong, S., Kim, Y., Han, J.: 2015, *Space Weather* **13**, 104. DOI.
- Jiang, C., Feng, X.: 2013, *Astrophys. J.* **769**, 144. DOI.

- Jones, S.I., Davila, J.M., Uritsky, V.: 2016, *Astrophys. J.* **820**, 113. DOI.
- Kim, T.K., Pogorelov, N.V., Borovikov, S.N., Jackson, B.V., Yu, H.S., Tokumaru, M.: 2014, *J. Geophys. Res. Space Phys.* **119**, 7981. DOI.
- Kojima, M., Tokumaru, M., Fujiki, K., Hayashi, K., Jackson, B.V.: 2007, *Astron. Astrophys.* **26**, 467. DOI.
- Koutchmy, S., Lamy, P.L.: 1985, *The f-Corona and the Circum-Solar Dust Evidences and Properties* **85**, Cambridge University Press, Cambridge 63. DOI.
- Kramar, M., Airapetian, V., Mikić, Z., Davila, J.: 2014, *Solar Phys.* **289**, 2927. DOI.
- Lee, C., Luhmann, J., Hoeksema, J., Sun, X., Arge, C., de Pater, I.: 2011, *Solar Phys.* **269**, 367. DOI.
- Levine, R.H., Schulz, M., Frazier, E.N.: 1982, *Solar Phys.* **77**, 363. DOI.
- Linker, J.A., Mikić, Z., Biesecker, D.A., Forsyth, R.J., Gibson, S.E., Lazarus, A.J., Lecinski, A., Riley, P., Szabo, A., Thompson, B.J.: 1999, *J. Geophys. Res. Space Phys.* **104**, 9809. DOI.
- Liu, Y., Hoeksema, J., Scherrer, P., Schou, J., Couvidat, S., Bush, R., Duvall, T., Hayashi, K., Sun, X., Zhao, X.: 2012, *Solar Phys.* **279**, 295. DOI.
- Lugaz, N., Manchester, W.B., Gombosi, T.I.: 2005, *Astrophys. J.* **634**, 651. DOI.
- MacNeice, P.: 2009, *Space Weather* **7**, 1. DOI.
- McComas, D.J., Elliott, H.A., Gosling, J.T., Skoug, R.M.: 2006, *Geophys. Res. Lett.* **33**, L09102. DOI.
- Mikic, Z., Linker, J.A., Schnack, D.D., Lionello, R., Tarditi, A.: 1999, *Phys. Plasmas* **6**, 2217. DOI.
- Morgan, H.: 2015, *Astrophys. J. Suppl.* **219**, 23. DOI.
- Newkirk, G., Fisk, L.A.: 1985, *J. Geophys. Res. Space Phys.* **90**, 3391. DOI.
- Odstroil, D.: 2003, *Adv. Space Res.* **32**, 497. DOI.
- Owens, M.J., Challen, R., Methven, J., Henley, E., Jackson, D.R.: 2013, *Space Weather* **11**, 225. DOI.
- Owens, M.J., Spence, H.E., McGregor, S., Hughes, W.J., Quinn, J.M., Arge, C.N., Riley, P., Linker, J., Odstroil, D.: 2008, *Space Weather* **6**, S08001. DOI.
- Patoul, J.d., Foullon, C., Riley, P.: 2015, *Astrophys. J.* **814**, 68. DOI.
- Quémerais, E., Lamy, P.: 2002, *Astron. Astrophys.* **393**, 295. DOI.
- Reiss, M.A., Temmer, M., Veronig, A.M., Nikolic, L., Vennerstrom, S., Schöngassner, F., Hofmeister, S.J.: 2016, *Space Weather* **14**, 495. DOI.
- Riley, P., Linker, J.A., Arge, C.N.: 2015, *Space Weather* **13**, 154. DOI.
- Riley, P., Lionello, R.: 2011, *Solar Phys.* **270**, 575. DOI.
- Riley, P., Linker, J., Mikic, Z., Lionello, R., Ledvina, S.A., Luhmann, J.G.: 2006, *Astrophys. J.* **653**, 1510. DOI.
- Riley, P., Lionello, R., Linker, J., Mikic, Z., Luhmann, J., Wijaya, J.: 2011, *Solar Phys.* **274**, 361. DOI.
- Riley, P., Ben-Nun, M., Linker, J., Mikic, Z., Svalgaard, L., Harvey, J., Bertello, L., Hoeksema, T., Liu, Y., Ulrich, R.: 2014, *Solar Phys.* **289**, 769. DOI.
- Schatten, K.H., Wilcox, J.M., Ness, N.F.: 1969, *Solar Phys.* **6**, 442. DOI.
- Schulz, M., Frazier, E.N., Boucher, D.J.: 1978, *Solar Phys.* **60**, 83. DOI.
- Shen, F., Feng, X., Xiang, C.: 2012, *J. Atmos. Solar-Terr. Phys.* **77**, 125. DOI.
- Shen, F., Feng, X., Wu, S., Xiang, C.: 2007, *J. Geophys. Res. Space Phys.* **112**, A06109. DOI.
- Shen, F., Feng, X., Xiang, C., Song, W.: 2010, *J. Atmos. Solar-Terr. Phys.* **72**, 1008. DOI.
- Shen, F., Shen, C., Wang, Y., Feng, X., Xiang, C.: 2013, *Geophys. Res. Lett.* **40**, 1457. DOI.
- Shen, F., Shen, C., Zhang, J., Hess, P., Wang, Y., Feng, X., Cheng, H., Yang, Y.: 2014, *J. Geophys. Res. Space Phys.* **119**, 7128. DOI.
- Shen, F., Yang, Z., Zhang, J., Wei, W., Feng, X.: 2018, *Astrophys. J.* **866**, 18. DOI.
- Strachan, L., Panasyuk, A.V., Kohl, J.L., Lamy, P.: 2012, *Astrophys. J.* **745**, 51. DOI.
- Tokumaru, M., Kojima, M., Fujiki, K.: 2010, *J. Geophys. Res. Space Phys.* **115**, A04102. DOI.
- Tokumaru, M., Satonaka, D., Fujiki, K.i., Hayashi, K., Hakamada, K.: 2017, *Solar Phys.* **292**, 41. DOI.
- Tóth, G., van der Holst, B., Huang, Z.: 2011, *Astrophys. J.* **732**, 102. DOI.
- Van de Hulst, H.: 1950, *Bull. Astron. Inst. Neth.* **11**, 135.
- Wang, T., Davila, J.M.: 2014, *Solar Phys.* **289**, 3723. DOI.
- Wang, Y.-M., Sheeley, N.: 1990, *Astrophys. J.* **355**, 726. DOI.
- Wang, Y.M., Young, P.R., Muglach, K.: 2014, *Astrophys. J.* **780**, 103. DOI.
- Wei, F.S., Feng, X.S., Cai, H.C., Zhou, Q.J.: 2003, *J. Geophys. Res. Space Phys.* **108**, 1238. DOI.
- Wiegelmann, T., Petrie, G.J.D., Riley, P.: 2017, *Space Sci. Rev.* **210**, 249. DOI.
- Wiengarten, T., Kleimann, J., Fichtner, H., Cameron, R., Jiang, J., Kissmann, R., Scherer, K.: 2013, *J. Geophys. Res. Space Phys.* **118**, 29. DOI.
- Wintoft, P., Lundstedt, H.: 1997, *Phys. Chem. Earth* **22**, 617. DOI.
- Wintoft, P., Lundstedt, H.: 1999, *J. Geophys. Res. Space Phys.* **104**, 6729. DOI.
- Yang, Y., Shen, F., Yang, Z., Feng, X.: 2018, *Space Weather* **16**, 1227. DOI.
- Zhao, X., Dryer, M.: 2014, *Space Weather* **12**, 448. DOI.
- Zhao, X., Hoeksema, J.T.: 1995, *J. Geophys. Res. Space Phys.* **100**, 19. DOI.